ChemPubSoc Europe

DOI: 10.1002/ejic.201600511

EurJIC European Journal of Inorganic Chemistry

Full Paper

Metal Oxide Nanocrystals

The Ethylhexanoate Route to Metal Oxide Nanocrystals: Synthesis of CoO Nanooctahedra from Co^{II} 2-Ethylhexanoate

Mauro Epifani*[a] Peng-Yi Tang,[b,c] Aziz Genç,[b,d] Joan R. Morante,[c] Jordi Arbiol,[b,e] Raül Díaz,[f] and Susanne Wicker[g]

Abstract: CoO nanocrystals were prepared by solvothermal processing of Co 2-ethylhexanoate in oleylamine at 250 °C. The obtained products, identified as CoO by X-ray diffraction, had an octahedral shape, as seen by transmission electron microscopy, reflecting the cubic symmetry of the CoO crystallographic phase. The materials were converted into the Co_3O_4 phase after heat treatment at 400 °C. The nanocrystal evolution was investigated by FTIR spectroscopy. It was concluded that weak oleylamine bonding to the nanocrystal surface during the synthesis step favored the exchange with 2-ethylhexanoato ligands, and that the interplay between the two ligands favored the kinetic control of the growth, resulting in the finally observed octahedral morphology. The Co_3O_4 phase obtained from the heat treatment at 400 °C was used to process chemoresistive sensors, which were able to detect ethanol under dry and humid conditions (0 and 50 % r.h. H_2O at 25 °C) at low temperatures (100 °C).

Introduction

Carboxylate compounds like metal oleates are well-established precursors for the synthesis of metal oxide nanocrystals.[1] On the other hand, metal 2-ethylhexanoates are metal-organic compounds widely used as catalysts in many polymerization reactions,[2] but their use for the synthesis of metal oxide nanocrystals is much less exploited. Starting from the consideration that the metal–oxygen bond is already present in the 2-ethylhexanoate structure, as in metal oleates (and in other compounds like, for instance, metal nitrates[3]) we succeeded in synthesizing ZnO and SnO_2 nanocrystals by the decomposition of the related 2-ethylhexanoates in high-boiling amines.[4] Moreover, the same precursor was effective for the deposition of SnO_2 thin films.[5] Photo-decomposition of 2-ethylhexanoates has also been demonstrated to be applicable for preparing thin films[6] or nanoparticles.[7] This class of precursors hence seemed very versatile, and their presence for a large number of elements, coupled with low cost, air stability and low toxicity suggested to further explore their generality as metal oxide precursors. In fact, as stated above, there are still few works where they are exploited in such a way: these include intermetallic PtPb nanoparticles prepared by using lead(II) 2-ethylhexanoate,[8] CeO_2 and SnO_2 self-capped nanocrystals,[9] MoO_3 nanoparticles,[10] colloidal In-doped ZnO nanocrystals,[11] kersterite nanocrystals.[12] Extending this class of precursors is of interest for the many underlined practical advantages, but also from a fundamental point of view, for enlarging the body of knowledge related to nanochemistry precursors. In this work, we show the successful synthesis of CoO nanooctahedra by decomposition of Co 2-ethylhexanoate in oleylamine. The phase stability of the nanostructures was also investigated, showing that at 400 °C phase transformation to Co_3O_4 took place. Moreover, both CoO and Co_3O_4 are of remarkable interest for their fundamental physical properties and for many applications related, for instance, to energy storage.[13] Then the development of a simple and low-temperature nanocrystal synthesis is of remarkable interest. This achievement would complement existing procedures like molten salt[14] and combustion synthesis. The resulting materials were used for processing gas-sensing devices.

Results and Discussion

The as-prepared synthesis product was first analyzed by XRD. The related pattern is shown in Figure 1, where only the reflections of CoO in the cubic crystallographic phase were found

[a] *Consiglio Nazionale delle Ricerche – Istituto per la Microelettronica e Microsistemi (CNR – IMM), Via Monteroni c/o Campus Universitario, 73100 Lecce, Italy E-mail: mauro.epifani@le.imm.cnr.it www.imm.cnr.it*

[b] *Catalan Institute of Nanoscience and Nanotechnology (ICN2), CSIC and The Barcelona Institute of Science and Technology (BIST), Campus UAB, Bellaterra, 08193 Barcelona, Catalonia, Spain*

[c] *Catalonia Institute for Energy Research (IREC), Jardins de les Dones de Negre 1, Sant Adrià del Besòs, 08930 Barcelona, Catalonia, Spain*

[d] *Department of Metallurgy and Materials Engineering, Faculty of Engineering, Bartin University, 74100 Bartin, Turkey*

[e] *ICREA, Pg. Lluís Companys 23, 08010 Barcelona, Catalonia, Spain*

[f] *Electrochemical Processes Unit, IMDEA Energy Institute, Avda. Ramón de la Sagra 3, 28935 Móstoles, Spain*

[g] *Institute of Physical and Theoretical Chemistry, University of Tübingen, Auf der Morgenstelle 15, 72076 Tübingen, Germany*

Supporting information and ORCID(s) from the author(s) for this article are available on the WWW under http://dx.doi.org/10.1002/ejic.201600511.

(JCPDS card 43-1004). In particular, the intensity ratio between the (111) and (200) peaks was inverted with respect to the expected trend, indicating preferential growth of CoO, as confirmed by the TEM results below. Of course, similar intensity enhancement was observed for the (222) reflection at ca. 77.5°. No other phases were detected, demonstrating the purity of the as-prepared samples. After heat treatment at 400 °C, the CoO phase was completely converted into the Co_3O_4 spinel phase (JCPDS card 98-002-6720), in agreement with the known stability trends of cobalt oxide phases in air.

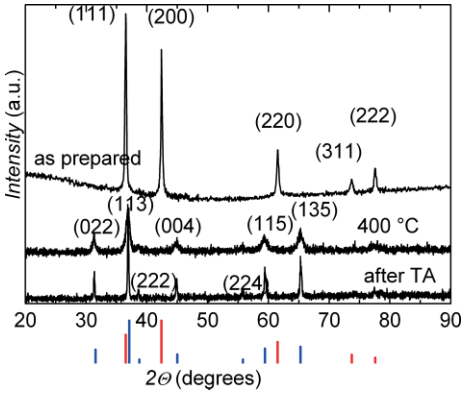

Figure 1. XRD patterns of the nanocrystals obtained under the indicated conditions. TA indicates the material collected after cooling from 900 °C during the thermal analyses. The theoretical intensities from CoO (red lines) and Co_3O_4 (blue lines) JCPDS cards are also reported.

Similar heat treatment under argon preserved the CoO phase (see the Supporting Information). The *a* lattice parameter of the rocksalt cubic structure of the as-prepared CoO sample was 4.2598(1) Å. The *a* lattice parameter of the spinel cubic structure of Co_3O_4 after heat treatment at 400 °C was 8.095(2) Å. These results are in very good agreement with those reported by other groups.[15]

The structure and morphology of the as-prepared CoO nanocrystals were investigated by high-resolution transmission electron microscopy (HRTEM) and annular dark field (ADF) scanning transmission electron microscopy (STEM) combined with electron energy loss spectroscopy (EELS) spectrum imaging (SI). Figure 2 shows the elemental composition measured by EELS on the nanocrystals evidenced in the right part of the image. The found atomic concentration values were 47 % for Co and 53 % for O, indeed confirming the CoO stoichiometry. Apparent oxygen excess is in agreement with the *p*-type semiconductor nature of CoO. Moreover, homogeneous distribution of both elements was clearly observed. Further HRTEM analyses, of which an example is reported in Figure 3, confirmed the $Fm\bar{3}m$ space group of the CoO nanoparticles.

Combined HAADF STEM and HRTEM studies helped us to model the 3D atomic morphology of the nanoparticles. In fact, every observed nanoparticle had an octahedral morphology defined by 8 (111) facets, as shown in the 3D atomic models on the bottom of Figure 3D. Atomic models of the nanoparticles were constructed using the Rhodius software,[16] which has been demonstrated to be very successful in the modeling of

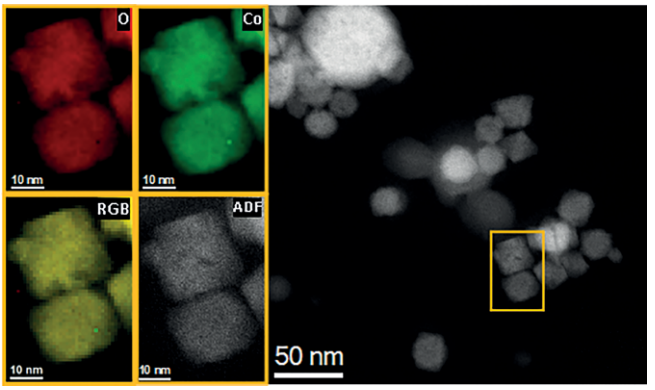

Figure 2. (right) ADF STEM micrograph showing typical octahedral as-prepared CoO nanoparticles in different projections. (left) EELS elemental maps for Co, O, combined RGB map and corresponding ADF STEM detail, obtained on the selected nanoparticles in the yellow squared region shown in the general view ADF STEM image on the right.

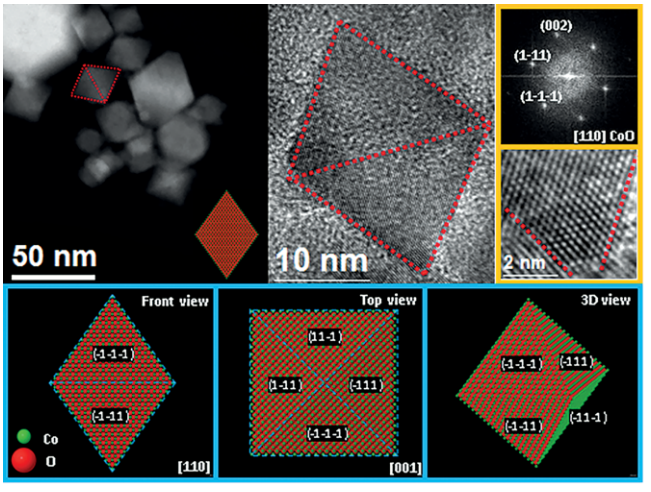

Figure 3. (top left) ADF STEM general view showing typical as-prepared CoO octahedral nanoparticles in different projections. The selected nanoparticle delimited with red pointed lines has been modeled in the inset. (top middle) HRTEM micrograph showing the projected facets of the octahedral CoO nanoparticle along the [110] zone axis. (top right) Power spectrum obtained on the previous HRTEM micrograph showing the cubic structure of the CoO nanoparticle along the [110] projection. The HRTEM below the power spectra shows an atomic resolution detail of the lateral facets of the octahedra corresponding to 111 planes. (bottom) Front ([110] projection), top ([001] projection) and 3D views of the octahedral nanoparticle model in the left, middle and right insets, respectively.

complex nanostructures.[17] These results are in agreement with the peak intensity ratios observed in the XRD pattern of Figure 1.

The effect of the heat treatment at 400 °C on the starting CoO nanocrystals is remarkable. As discussed below, this temperature was sufficient for *n*-oleylamine (OAm) removal; therefore, aggregation of the nanoparticles was expected. Moreover, the stoichiometry change and the remarkable lattice parameter increase (almost doubled) due to the phase transformation to Co_3O_4 (shown in Figure 1) imposed extensive reconstruction of the nanocrystals. In Figure 4 a representative image is shown,

demonstrating the phase transformation to Co_3O_4. In the Supporting Information another image is shown where the Co_3O_4 nanoparticles seem to be related to cubic regions during the transformation process. The smaller size with respect to the previous nanooctahedra is also to be noted. In fact, Rietveld refinement provided a mean size of ca. 35 nm, about half than that resulting from refinement of the as-prepared CoO sample.

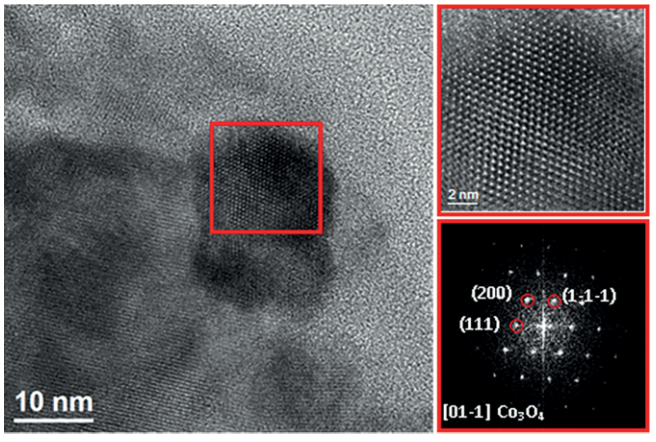

Figure 4. Left panel: general HRTEM micrograph of the CoO sample heat-treated at 400 °C. Right panel: detail structure of the red squared area is presented in the magnified TEM (left); the corresponding FFT spectrum (bottom) reveals these nanoparticles can be indexed to cubic (spinel) Co_3O_4, as visualized along the [01$\bar{1}$] direction.

This reconstruction process was probably responsible for the appreciable specific surface area of the sample, which – despite the 400 °C treatment – was 49 m^2/g by BET. This value compares well with the 29 m^2/g obtained by the urea combustion method,[15] the 65 m^2/g by complex decomposition,[18] and the 82 m^2/g by spray pyrolysis,[19] just to name a few. Only Co_3O_4 nanorods, but prepared at lower temperature (300 °C), displayed a much larger area (232 m^2/g).[20] The focus on the phase stability of the nanoparticles was necessary since sensing devices, which were the initial application aim, need high-temperature pretreatment for chemical, thermal and electrical stabilization before being operated. In particular, any organic residual should be removed from the sample. For this reason, DSC/TG measurements were carried out for selecting the proper heat-treatment temperature, which – as shown above – resulted to be 400 °C.

The results are shown in Figure 5. The data are dominated by two main phenomena: an intense exothermic peak associated with a sharp mass loss, centered at ca. 250 °C and that comprises a shoulder on the lower temperature flank, and a subsequent mass increase not associated with DSC peaks. The 250 °C peak was interpreted in terms of dissociation/oxidation of the oleylamine ligands bonded to the CoO nanocrystals, as shown by the FTIR data presented below. The subsequent mass increase suggested oxygen uptake from the atmosphere to form Co_3O_4, which is coherent with the sample mass surpassing the initial value. The involved temperature range is in agreement with the results of Figure 1. Slight mass decrease in the higher temperature range could be due to sample structural rearrangement. Bulk Co_3O_4 will convert into CoO only above 950 °C. In fact, the sample collected after thermal analysis displayed the Co_3O_4 XRD pattern (Figure 1), with remarkable peak narrowing due to the high temperature sintering. It is interesting to observe that the sample heated at 900 °C, as observed by SEM (see the Supporting Information), displayed some structures again resembling the cubic structure of CoO, despite at a much larger size imposed by the high temperature.

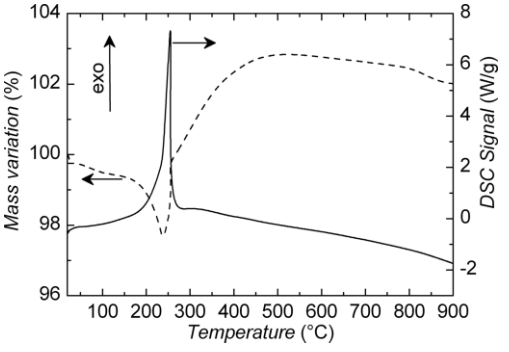

Figure 5. DSC/TG curves measured on the as-prepared CoO sample.

The sample evolution could be confirmed by FTIR investigation, which also provided further insight into the material formation pathways. The spectra recorded in various steps of the synthesis process are reported in Figure 6, together with those of Co 2-ethylhexanoate [$Co(EtEs)_2$] and OAm.

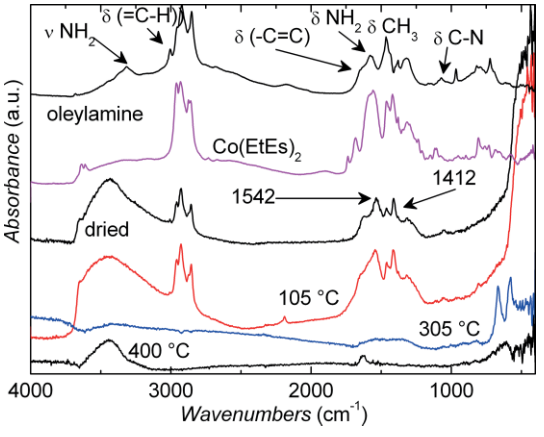

Figure 6. FTIR spectra measured on the indicated samples.

In the dried CoO nanocrystals, it is possible first of all to observe an intense and broad band below 3500 cm^{-1}, with a structure typical of the overlap of several OH moieties. Since the synthesis is nonaqueous, it could be speculated that the nanocrystal formation proceeds through the condensation of Co–OH bonds, but the reaction between OAm and $Co(EtEs)_2$ will require a specific investigation for being identified. It is worth mentioning that the reaction with oleic acid only provided a small amount of a waxy material. More interestingly, the investigation of the sample composition offers hints about a synergistic effect of OAm and 2-ethylhexanoato ligands in the synthesis of the final CoO nanocrystals. OAm has been used in the reaction with $Co(acac)_3$[21] in two different works, yielding

CoO but without the clear shape obtained in the present work. Different shapes were obtained by the decomposition of cobalt oleate in the presence of oleic acid.[22] Cobalt acetate decomposition in OAm only provided elemental Co nanocrystals, while large CoO octahedral particles were obtained in a mixture of OAm and oleic acid. In this case, the role of OAm was recognized as that of a reducing agent. Decomposition of $Co(acac)_2$ required a mixture of oleic acid, OAm and cetyltrimethylammonium bromide for obtaining octahedral nanocrystals. In earlier studies, decomposition of $Co(acac)_3$ in oleylamine had been used, with different shapes of the final CoO nanocrystals.[23] Coming to the present study, in the as-prepared sample the $\nu(NH_2)$ band at ca. 3300 cm^{-1} is hidden by the OH band, but the presence of OAm is nevertheless ensured by a very weak δ(C–H) band at 3004 cm^{-1}, the δ(–C=C) band at ca. 1645 cm^{-1} (the Co precursor does not have any band in that region) and further $\delta(NH_2)$ and δ(C–N) persistence. The $\delta(CH_3)$ band at ca. 1465 cm^{-1} is not indicative since it receives a contribution even from any 2-ethylhexanoate residual. On the other hand, the OAm signal is quite weak, and suggests that its bonding to the CoO surface is not strong enough to survive the washing steps. In fact, the mass loss in the thermal analysis associated with oleylamine desorption (ca. 2 %, see Figure 5) was very limited. An important feature is a couple of new bands at ca. 1542 and 1412 cm^{-1}. These bands, due to asymmetric and symmetric carboxylate stretching modes, respectively, are typical of the coordination of a carboxylic acid to a metal ion.[24] They are accompanied by the disappearance of the carbonyl band of the free acid at ca. 1740 cm^{-1}. In fact, the spectrum of the Co precursor contained a band at 1740 cm^{-1}, which was not observed anymore in the dried sample. From the 130 cm^{-1} value of Δ, the separation between the carboxylate stretching modes, we can deduce that the bonding is of a chelating type.[24,25] Summarizing: The CoO surface is coordinated with OAm and 2-ethylhexanoato moieties, the latter in chelating configuration; but the OAm bonding to the nanocrystal surface is weak and can be easily substituted during the growth by the 2-ethylhexanoato ligands generated by $Co(EtEs)_2$. The dynamic interplay between the two ligands originates the peculiar shape of the nanocrystals. By "peculiar" we do not mean that it is an unexpected shape, being closely related to the crystal symmetry of CoO, but that the combination of the two ligands is tuned in such a way to provide the proper kinetic control over the growth, allowing such stable crystallographic habit to emerge. The spectra for 105 °C and 305 °C, soon before and after the intense exothermic peak discussed in Figure 5, confirm the interpretation of the thermal analysis data. After heating at 105 °C, the IR signal is identical to that of the as-prepared sample, since the exothermic phenomena have not begun yet. Instead, at 305 °C, after the peak completion, the IR signal drastically changed in the region characterized by OAm and 2-ethylhexanoate modes. This result confirms that the exothermic peak was due to organics desorption/decomposition. It should be noted that the intense bands at ca. 1500 cm^{-1} were substituted by broad and weak bands, showing that some species are still present. They could be partly responsible for the slightly mass decrease at high temperatures observed in Figure 5. After 400 °C, no signals were observed apart from OH, water and typical oxide modes at low wavenumbers, indicating complete thermal and chemical stabilization of the material.

The gas-sensing properties of the prepared sensor was evaluated towards three different gases (CH_4, CO, and EtOH). The raw resistance data of the measurement are plotted in Figure 7, showing typical *p*-type behavior through resistance increase during exposure to reducing gases. The corresponding response data are reported in Table 1. It can be seen, that the Co_3O_4 sensor responses to all three gases under dry conditions, but is rather selective to ethanol in humidity (50 % r.h. H_2O at 25 °C). In general, the highest response was obtained to this gas. If we focus on the ethanol sensing, the response data are not comparable with those recently reported.[26] They are more comparable, but still smaller than those obtained with various Co_3O_4 morphologies.[26b,27] The comparison is more useful if the related operating temperatures are considered. While in the literature they are easily higher than 200 °C[28] and up to 300 °C,[29] in our case the highest response was observed at 100 °C and not at higher temperatures, indicating that the Co_3O_4 prepared by this procedure is suitable for low-temperature gas detection. This result compensates the relatively low responses obtained. The lowered response to CH_4 and CO in humid air indicates that these gases are competing with H_2O for the same adsorption sites more than EtOH.

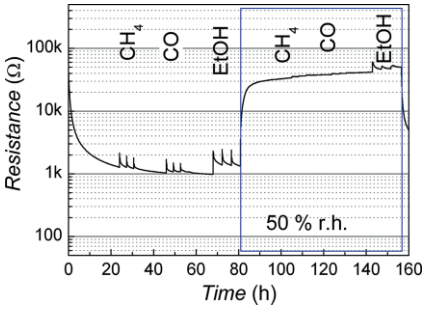

Figure 7. Resistance measurement of a Co_3O_4 sensor at 100 °C under CH_4 (500, 1000, and 2000 ppm), CO (20, 50, and 100 ppm), and EtOH (45, 90, and 170 ppm) exposure in dry and humid synthetic air background (0 and 50 % r.h. H_2O at 25 °C).

Table 1. Response data at the operating temperature of 100 °C calculated from the curves in Figure 7.

Test gas		Response	Response	Response
CH_4	ppm	500	1000	2000
	r.h. 0 %	1.7	1.5	1.4
	r.h. 50 %	1.0	1.0	1.0
CO	ppm	20	50	100
	r.h. 0 %	1.5	1.4	1.4
	r.h. 50 %	1.0	1.0	1.0
EtOH	ppm	45	90	170
	r.h. 0 %	2.4	2.3	2.4
	r.h. 50 %	1.5	1.2	1.3

Conclusions

It is possible to extend the applicability of metal 2-ethylhexanoates as precursors for the synthesis of metal oxide nanostruc-

tures. Cobalt 2-ethylhexanoate is in fact a convenient precursor for the synthesis of CoO nanostructures, likely through the reaction of oleylamine with 2-ethylhexanoate ligands. The resulting nanocrystals have the shape of nanooctahedra, related to the crystal phase of CoO, and are converted into Co_3O_4 upon high-temperature treatment, in agreement with the analogous phase transformations of bulk CoO. The resulting materials are suitable for processing low-temperature chemical gas sensors.

Experimental Section

In a typical synthesis, 1 g of Co 2-ethylhexanoate (65 % in mineral spirits, Strem Chemicals; in the following denoted as $CoEtEs_2$) was dissolved in 10 mL of *n*-oleylamine (OAm, 70 %, Sigma–Aldrich) in a 16 mL glass vial. Then the vial was placed into a 45 mL steel autoclave (Parr), the autoclave was heated up to 250 °C in a muffle furnace at a rate of 5 °C/min and kept at that temperature for 2 h. After cooling, the product was extracted with methanol, washed with acetone, and dried at 90 °C. A dark-brownish powder was obtained (this sample will be referred to as "dried" or "as-prepared"). The powders were heat-treated at 400 °C in air for 1 h for thermal and phase stabilization before the sensing device processing. Samples were also heat-treated at 105 °C and 305 °C for 15 min for investigating the sample evolution during the thermal treatment.

X-ray diffraction (XRD) was carried out with a Panalytical X'Pert PRO-MPD diffractometer working with Cu-K_α radiation (λ = 1.5406 Å) using a Bragg–Brentano geometry. Rietveld refinement of the XRD patterns was carried out with the Maud software.[30]

Fourier transform infrared (FTIR) measurements were carried out with a Nicolet 6700 spectrometer in diffuse reflectance setup after dispersing the sample powders in KBr.

Thermal analyses were carried out with a thermal balance model SDT Q-600 from TA instruments under an air flow of 100 mL/min and a thermal ramp of 10 °C/min.

High-resolution transmission electron microscopy (HRTEM) analyses of the powders were carried out with a field emission gun microscope FEI Tecnai F20, working at 200 keV with a point-to-point resolution of 0.19 nm. Scanning transmission electron microscopy (STEM) in annular dark field (ADF) mode combined with electron energy loss spectroscopy (EELS) spectrum imaging (SI) were also obtained in the same FEI Tecnai F20 instrument.

Brunauer–Emmett–Teller (BET) single point specific surface area measurement on the sample heated in air at 400 °C was performed with an Autochem II 2920 Micrometrics, equipped with a TCD detector. Before the measurement the sample was outgassed at 300 °C under an He flow for 2 h.

The gas-sensing device was prepared out of the 400 °C pre-heated powder. A suspension of this powder and 2-propanol was drop-coated onto an alumina substrate (25.4 mm × 4.2 mm × 0.6 mm), which was provided with interdigitated Pt-electrodes for resistance read-out on the front side and a Pt-heater for temperature control on the back side. During the drop-coating process the substrate was placed on a hot plate and heated to ca. 60 °C. Then it was annealed in a four-zone moving belt oven at 400 °C. The gas sensing tests were done by measuring the resistance changes of the obtained gas sensor with a Keithley 199 multimeter in operando at different temperatures 100–200 °C. For supplying different concentrations of CH_4 (500, 1000, and 2000 ppm), CO (20, 50, and 100 ppm), and EtOH (45, 90, and 170 ppm) under both dry and humid background conditions (0 and 50 % r.h. H_2O at 25 °C) a computer-controlled gas mixing system, equipped with mass flow controllers and data acquisition cards was used. The sensor response was defined as $(R_{gas} - R_0)/R_0$, where R_0 is the sensor baseline electrical resistance in synthetic air and R_{gas} indicates the sensor electrical resistance after equilibration in the target gas.

Acknowledgments

The authors acknowledge the SOLAR project (DM19447). We thank Fernando Pico for the XRD measurements, Giovanni Battista Pace for the help with the sample preparation, Teresa Andreu and Marta M. Natile for additional characterizations. Funding is acknowledged from the Generalitat de Catalunya (2014 SGR 1638) and the Spanish Ministry of Economy and Competitiveness (MINECO) coordinated projects between the Catalonia Institute for Energy Research (IREC), the Catalan Institute of Nanoscience and Nanotechnology (ICN2) (TNT-FUELS, e-TNT) (MAT2014-59961-C2-2-R), and the Severo Ochoa Excellence Program. Part of the present work has been performed in the framework of the Universitat Autònoma de Barcelona Materials Science PhD program.

Keywords: Nanoparticles · Oxide nanocrystals · Solvothermal processing · Cobalt · Sensors

[1] Y. W. Jun, J. S. Choi, J. Cheon, *Angew. Chem. Int. Ed.* **2006**, *45*, 3414–3439; *Angew. Chem.* **2006**, *118*, 3492–3517.
[2] a) N. N. Glebova, N. N. Kostitsyna, O. K. Sharaev, V. A. Yakovlev, *Polym. Sci., Ser. B* **2006**, *48*, 237–239; b) C. M. Kuo, S. J. Clarson, *J. Inorg. Organomet. Polym. Mater.* **2012**, *22*, 577–587; c) H. Lee, S. Do, S. Lee, H. Kim, C. Bae, S. Jung, B. Y. Lee, G. Kwag, *Polymer* **2014**, *55*, 6483–6487; d) Z. M. Li, G. P. Yan, C. W. Ai, Q. Zhang, L. Li, F. Liu, X. H. Yu, B. A. Zhao, *J. Appl. Polym. Sci.* **2012**, *124*, 3704–3713; e) T. Sadik, V. Massardier, F. Becquart, M. Taha, *Polymer* **2012**, *53*, 4585–4594; f) M. Winkler, T. M. Lacerda, F. Mack, M. A. R. Meier, *Macromolecules* **2015**, *48*, 1398–1403.
[3] D. S. Wang, T. Xie, Q. Peng, S. Y. Zhang, J. Chen, Y. D. Li, *Chem. Eur. J.* **2008**, *14*, 2507–2513.
[4] M. Epifani, J. Arbiol, R. Diaz, M. J. Peralvarez, P. Siciliano, J. R. Morante, *Chem. Mater.* **2005**, *17*, 6468–6472.
[5] M. Epifani, L. Francioso, P. Siciliano, A. Helwig, G. Mueller, R. Diaz, J. Arbiol, J. R. Morante, *Sens. Actuators B* **2007**, *124*, 217–226.
[6] a) L. S. Andronic, R. H. Hill, *J. Photochem. Photobiol. A* **2002**, *152*, 259–265; b) H. H. Park, X. Zhang, S. W. Lee, D. J. Jeong, S. M. Lee, K. D. Kim, D. G. Choi, J. H. Choi, J. Lee, E. S. Lee, H. K. Kang, H. H. Park, R. H. Hill, J. H. Jeong, *Microelectron. Eng.* **2011**, *88*, 923–928; c) H. H. Park, X. Zhang, S. W. Lee, K. D. Kim, D. G. Choi, J. H. Choi, J. Y. Lee, E. S. Lee, H. H. Park, R. H. Hill, J. H. Jeong, *J. Mater. Chem.* **2011**, *21*, 657–662; d) S. Tradel, G. Z. Li, X. Zhang, R. H. Hill, *J. Photopolym. Sci. Technol.* **2006**, *19*, 467–475; e) H. J. Zhu, R. H. Hill, *J. Non-Cryst. Solids* **2002**, *311*, 174–184.
[7] R. J. de Oliveira, P. Brown, G. B. Correia, S. E. Rogers, R. Heenan, I. Grillo, A. Galembeck, J. Eastoe, *Langmuir* **2011**, *27*, 9277–9284.
[8] L. R. Alden, D. K. Han, F. Matsumoto, H. D. Abruna, F. J. DiSalvo, *Chem. Mater.* **2006**, *18*, 5591–5596.
[9] Y. J. Kim, Y. S. Kim, S. Y. Chai, D. H. Cha, Y. S. Choi, W. I. Lee, *New J. Chem.* **2007**, *31*, 260–264.
[10] E. D. Santos, F. A. Sigoli, I. O. Mazali, *J. Solid State Chem.* **2012**, *190*, 80–84.
[11] X. Y. Liang, Y. P. Ren, S. Bai, N. Zhang, X. L. Dai, X. Wang, H. P. He, C. H. Jin, Z. Z. Ye, Q. Chen, L. W. Chen, J. P. Wang, Y. Z. Jin, *Chem. Mater.* **2014**, *26*, 5169–5178.
[12] G. Gabka, P. Bujak, M. Gryszel, A. Ostrowski, K. Malinowska, G. Z. Zukowska, F. Agnese, A. Pron, P. Reiss, *Chem. Commun.* **2015**, *51*, 12985–12988.

[13] a) M. V. Reddy, G. V. Subba Rao, B. V. R. Chowdari, *Chem. Rev.* **2013**, *113*, 5364–5457; b) H. Guan, X. Wang, H. Q. Li, C. Y. Zhi, T. Y. Zhai, Y. Bando, D. Golberg, *Chem. Commun.* **2012**, *48*, 4878–4880.
[14] a) M. V. Reddy, Z. Beichen, K. P. Loh, B. V. R. Chowdari, *CrystEngComm* **2013**, *15*, 3568–3574; b) M. V. Reddy, Z. Beichen, L. J. e. Nicholette, Z. Kaimeng, B. V. R. Chowdari, *Electrochem. Solid-State Lett.* **2011**, *14*, A79–A82.
[15] M. V. Reddy, G. Prithvi, K. P. Loh, B. V. Chowdari, *ACS Appl. Mater. Interfaces* **2014**, *6*, 680–690.
[16] S. Bernal, F. J. Botana, J. J. Calvino, C. Lopez-Cartes, J. A. Perez-Omil, J. M. Rodriguez-Izquierdo, *Ultramicroscopy* **1998**, *72*, 135–164.
[17] a) R. R. Zamani, M. Ibáñez, M. Luysberg, N. García-Castelló, L. Houben, J. D. Prades, V. Grillo, R. E. Dunin-Borkowski, J. R. Morante, A. Cabot, J. Arbiol, *ACS Nano* **2014**, *8*, 2290–2301; b) M. de la Mata, C. Magén, P. Caroff, J. Arbiol, *Nano Lett.* **2014**, *14*, 6614–6620; c) J. Arbiol, A. Cirera, F. Peiró, A. Cornet, J. R. Morante, J. J. Delgado, J. J. Calvino, *Appl. Phys. Lett.* **2002**, *80*, 329–331.
[18] S. Farhadi, K. Pourzare, *Mater. Res. Bull.* **2012**, *47*, 1550–1556.
[19] Z. W. Zhao, K. Konstantinov, L. Yuan, H. K. Liu, S. X. Dou, *J. Nanosci. Nanotechnol.* **2004**, *4*, 861–866.
[20] G. X. Wang, X. P. Shen, J. Horvat, B. Wang, H. Liu, D. Wexler, J. Yao, *J. Phys. Chem. C* **2009**, *113*, 4357–4361.
[21] a) X. M. He, X. Y. Song, W. Qiao, Z. W. Li, X. Zhang, S. M. Yan, W. Zhong, Y. W. Du, *J. Phys. Chem. C* **2015**, *119*, 9550–9559; b) X. M. He, W. Zhong, S. M. Yan, C. Liu, H. G. Shi, C. T. Au, Y. W. Du, *J. Phys. Chem. C* **2014**, *118*, 13898–13903.
[22] M. R. Buck, A. J. Biacchi, R. E. Schaak, *Chem. Mater.* **2014**, *26*, 1492–1499.
[23] a) J. F. Liu, S. Yin, H. P. Wu, Y. W. Zeng, X. R. Hu, Y. W. Wang, G. L. Lv, J. Z. Jiang, *J. Phys. Chem. B* **2006**, *110*, 21588–21592; b) W. S. Seo, J. H. Shim, S. J. Oh, E. K. Lee, N. H. Hur, J. T. Park, *J. Am. Chem. Soc.* **2005**, *127*, 6188–6189.
[24] D. H. Lee, R. A. Condrate, *J. Mater. Sci.* **1999**, *34*, 139–146.
[25] W. W. Yu, Y. A. Wang, X. G. Peng, *Chem. Mater.* **2003**, *15*, 4300–4308.
[26] a) C. S. Lee, Z. F. Dai, S. Y. Jeong, C. H. Kwak, B. Y. Kim, D. H. Kim, H. W. Jang, J. S. Park, J. H. Lee, *Chem. Eur. J.* **2016**, *22*, 7102–7107; b) S. Wicker, K. Grossmann, N. Barsan, U. Weimar, *Sensor Actuat. B-Chem.* **2013**, *185*, 644–650.
[27] a) J. M. Xu, J. Zhang, B. B. Wang, F. Liu, *J. Alloys Compd.* **2015**, *619*, 361–367; b) Z. Wen, L. P. Zhu, W. M. Mei, L. Hu, Y. G. Li, L. W. Sun, H. Cai, Z. Z. Ye, *Sensor Actuat. B-Chem.* **2013**, *186*, 172–179.
[28] Q. Z. Jiao, M. Fu, C. You, Y. Zhao, H. S. Li, *Inorg. Chem.* **2012**, *51*, 11513–11520.
[29] a) P. P. Zhang, J. W. Wang, X. X. Lv, H. Zhang, X. H. Sun, *Nanotechnology* **2015**, *26*(27), article no. 275501; b) K.-I. Choi, H.-R. Kim, K.-M. Kim, D. Liu, G. Cao, J.-H. Lee, *Sensors Actuators B: Chem.* **2010**, *146*, 183–189.
[30] L. Lutterotti, *Maud*, version 2.33, University of Trento, **2011**, http://maud.radiographema.eu/.

Received: May 2, 2016
Published Online: July 29, 2016